Journal of Biomedical Optics

BiomedicalOptics.SPIEDigitalLibrary.org

Feasibility study: protein denaturation and coagulation monitoring with speckle variance optical coherence tomography

Changho Lee
Gyeongwoo Cheon
Do-Hyun Kim
Jin U. Kang

SPIE.

Changho Lee, Gyeongwoo Cheon, Do-Hyun Kim, Jin U. Kang, "Feasibility study: protein denaturation and coagulation monitoring with speckle variance optical coherence tomography," *J. Biomed. Opt.* **21**(12), 125004 (2016), doi: 10.1117/1.JBO.21.12.125004.

Feasibility study: protein denaturation and coagulation monitoring with speckle variance optical coherence tomography

Changho Lee,[a,*] Gyeongwoo Cheon,[a] Do-Hyun Kim,[b] and Jin U. Kang[a]
[a]Johns Hopkins University, Department of Electrical and Computer Engineering, 3400 North Charles Street, Baltimore, Maryland 21218, United States
[b]U.S. Food and Drug Administration, Center for Devices and Radiological Health, 10903 New Hampshire Avenue, Silver Spring, Maryland 20993, United States

Abstract. We performed the feasibility study using speckle variance optical coherence tomography (SvOCT) to monitor the thermally induced protein denaturation and coagulation process as a function of temperature and depth. SvOCT provided the depth-resolved image of protein denaturation and coagulation with microscale resolution. This study was conducted using egg white. During the heating process, as the temperature increased, increases in the speckle variance signal was observed as the egg white proteins coagulated. Additionally, by calculating the cross-correlation coefficient in specific areas, denaturized egg white conditions were successfully estimated. These results indicate that SvOCT could be used to monitor the denaturation process of various proteins. [DOI: 10.1117/1.JBO.21.12.125004]

Keywords: denaturation; coagulation; optical coherence tomography; speckle variance.

Paper 160603R received Aug. 31, 2016; accepted for publication Nov. 14, 2016; published online Dec. 10, 2016.

1 Introduction

Biological tissues consist of various large polymers such as proteins, lipids, and carbohydrates. In particular, proteins are vital components that are responsible for maintaining physiological activities such as chemical reactions, cell activities, immune responses, and so on.[1,2] Normally, proteins remain as stable three-dimensional structures with their specific functions. When external stress such as strong acid, radiation, and heat is applied to proteins, their stable structure experiences transformation. This phenomenon is called denaturation, which induces disruptions of activities and changes of physical properties of biological tissue.[3,4] Therefore, the ability to assess the state of protein denaturation and coagulation would offer crucial physiological information. Although various techniques have been investigated for monitoring the protein denaturation process by measuring biochemical reaction, heat capacity, differential absorbance of polarized light, thermal conductivity, etc., the studies focused on investigating the detection of limited conformational variance in the protein.[5–8]

There are new approaches to monitor the denaturation process based on conventional imaging techniques such as magnetic resonance imaging (MRI), ultrasound imaging (USI), and florescence spectroscopy (FRS).[9–11] These techniques have advantages and disadvantages for monitoring the denaturation process. For instance, MRI can show a large field of view with high contrast; however, MRI requires long-time data acquisition and is relatively costly. USI enables us to provide real-time acoustic imaging and has relatively low cost; however, low resolution and coupling medium (i.e., water and gel) are the drawbacks. FRS has high spatial resolution and spectroscopic information, but requires additional contrast agents for labeling samples and is limited to visualizing the depth-resolved information.

Optical coherence tomography (OCT) is a powerful optical imaging technique for visualizing microscale cross-sectional morphological and functional tissue characteristics without sacrificing biological tissue.[12] Thanks to its high spatial resolution, high-speed imaging, and highly flexible setup, it has become a main tool for diverse medical diagnosis fields such as ophthalmology, dermatology, oncology, and gastroenterology.[13–17] Moreover, these advantages also have an important role in being adaptable for nondestructive inspections for various thin-layered products, monitoring material conditions, and basic science research.[18–21] OCT techniques have been especially used to monitor the changes to biological tissues under external stress. For instance, Choi et al.[22] monitored the freezing of biological tissue during cryosurgery. Greco et al.[23] estimated the collapse temperature of pharmaceutical formulations under a freeze and drying process. Koinzer et al.[24] compared both retinal temperature rise and OCT legion classes of retina during laser irradiation. Those approaches, which observed tissue property changes through OCT images, used thermal coupler and optoacoustic measurements to determine and calibrate the tissue temperature information. As an alternative method, Seevaratnam et al.[25] reported envelope statistics for OCT signals to quantify temperature changes of a phantom under a heating condition. Another method used the phase information from the OCT imaging. Spahr et al.[26] reported phase sensitive OCT for photothermal expansion imaging in a multilayered phantom with an absorber under laser irradiation. This technique was usually utilized in photothermal imaging with a specific absorber (i.e., gold nanorod).[27]

*Address all correspondence to: Changho Lee, E-mail: ch31037@gmail.com

1083-3668/2016/$25.00 © 2016 SPIE

Speckle variance optical coherence tomography (SvOCT) has recently received the spotlight as a new microangiography technique for mapping microvasculatures in specific-depth blood vessels without contrast agents.[28] In principle, the changes of speckle pattern with time induced by moving molecules in biological tissue can be quantitatively acquired by estimating speckle variances between frames or lines.[29]

In this paper, we aim to demonstrate the feasibility of SvOCT as a protein denaturation and coagulation process-monitoring method. This approach is based on the fact that when an external stimulation is applied to a biological tissue, speckle pattern changes in SvOCT image can be observed. These changes can be detected and quantitatively analyzed to quantify the state of protein denaturation. To understand the heat diffusion and the temperature gradient in our setup, we performed the finite-difference time-domain (FDTD) modeling. By applying heat to the aluminum housing containing egg white, we monitored and analyzed temperature distribution within the egg white. The transformation of egg white was analyzed by two quantitative methods: (1) speckle variances analysis and (2) cross-correlation analysis of different regions of interest (ROIs) from SvOCT images at different heating temperatures.

2 Experimental Setup and Materials

2.1 *OCT System Setup*

To perform speckle variance OCT imaging, an in-house developed swept source optical coherence tomography system was used (Fig. 1). A commercial swept source original equipment manufacturer (OEM) engine (Axsun Technologies, Inc.) with a center wavelength of ~1060 nm, full width sweeping bandwidth of ~100 nm, and repetition rate of 100 kHz was used in the system. As shown in Fig. 1, the laser output was coupled to a 75:25 optical fiber coupler (TW1064R3A2A, Thorlabs). Twenty-five percentage of the laser was focused on a sample with an objective lens (AC127-019-C, Thorlabs); 75% of the laser went to a transmissive reference arm. Polarization controllers (FPC020, Thorlabs) were utilized to match the polarization conditions of both arms. The reference and signal were mixed by a 50:50 coupler and detected by a balanced detector. The mixed signal was digitalized by a high-speed digitizer (500 MSPS, 12-bit resolution) imbedded in the OEM engine and captured by a frame grabber (PCIe-1433, National Instruments). Parallel processing with a graphics processing unit (GTX590, NVIDIA) was used for high-speed imaging processing, including fast fourier transform (FFT) and background noise removal.[30,31] B-scan OCT images composed of 1024 × 1024 pixels along X- and Z-axes, respectively, were displayed at a frame rate of 100 Hz. A galvo scanner (GVS001, Thorlabs) was used for B-scan OCT imaging. The scanning range was 300 μm. The output power from the sample probe was ~2.5 mW. The measured spatial resolutions were 6.7 μm axially and 8.5 μm laterally. The field of depth was approximately 890 μm. The number of 100 B-scan OCT images was recorded at the same scanning region during approximately 1 s. After receiving the OCT raw data, we processed and extracted speckle variances and correlation values.

2.2 *Experimental Conditions*

Carefully separated normal egg white from egg yolk, which contains about 10% proteins in weight, was prepared in an aluminum small bowl to monitor its denaturation process. A hot plate (Fisher Scientific, 11-100-100H) and an IR thermometer (FLIR TG165, FLIR) were used to heat the sample and to monitor temperature changes in the sample. Although imaging was done continuously during the heating process, the sample was analyzed at 16 different temperatures: 53.4°C, 56.1°C, 59.0°C, 61.5°C, 64.9°C, 67.6°C, 70.3°C, 76.4°C, 78.4°C, 81.8°C, 83.8°C, 85.1°C, 87.4°C, 89.1°C, 91.7°C, and 92.2°C. We measured the sample temperature using an FLIR infrared thermometer at 30 s interval while acquiring OCT data.

2.3 *FDTD Simulation Setup*

To conduct the FDTD modeling for estimating heat transfer and temperature distribution in our setup, we used the COMSOL (COMSOL 5.1, COMSOL, Inc.) program. We simplified the simulation by ignoring one of the transverse direction due to the symmetry of our experimental setup. Figure 2(a) shows the two-dimensional simulated structure, which includes an aluminum bowl, egg white, and air. We assumed that the heat is induced evenly along the bottom line. The dimension of the aluminum bowl (medium 1) is 12 (width) × 8 (height) mm, and has an inner rectangular space that has 8 (width) × 2 (height) mm from the top surface. The egg white medium was located in the inner space of the aluminum bowl (medium 2) with 8 (width) × 1 (height) mm. The outside is regarded as air. Table 1 shows the design parameters of FDTD simulation. The values (i.e., heat capacity, thermal conductivity, and density) of aluminum came from the COMSOL library. The values of egg white were obtained from Ref. 32. Because the above parameter values of egg white are varied by different temperature

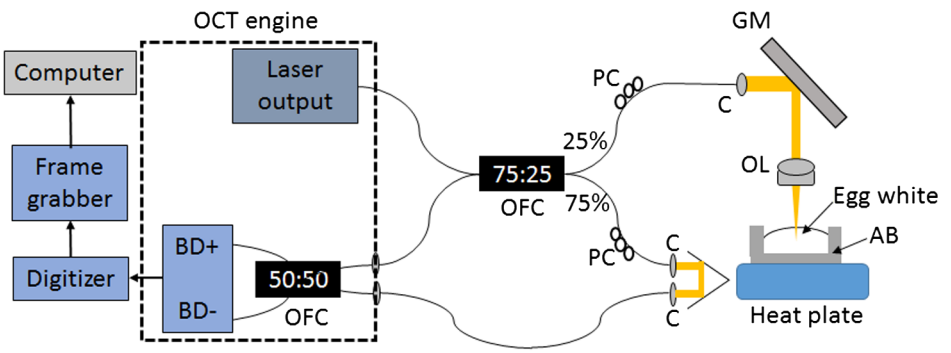

Fig. 1 Schematic of SvOCT setup. GM, galvo meter; C, collimator; OL, objective lens; AB, aluminum small bowl; PC, polarization controller; BD, balance detector; and OFC, optical fiber coupler.

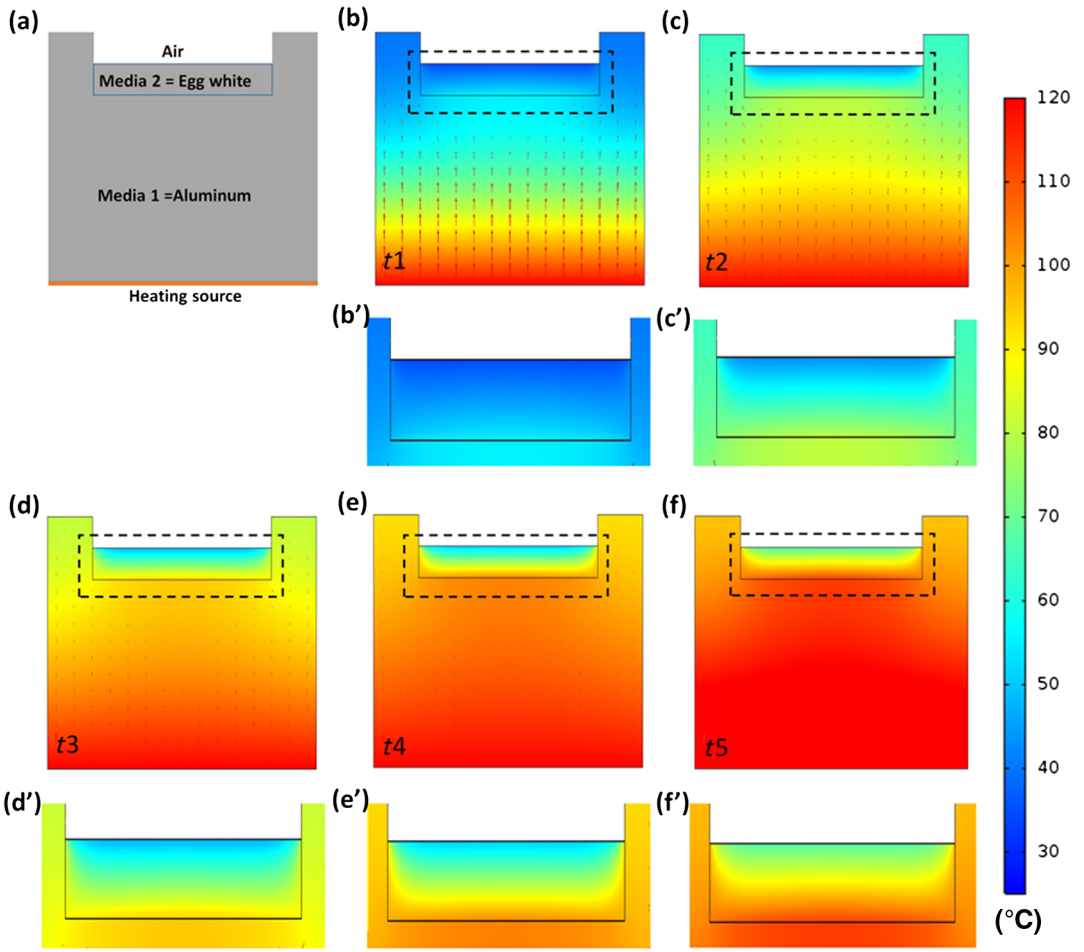

Fig. 2 FDTD simulation results. (a) Designed two-dimensional structure. (b)–(f) Simulation results of temperature distribution at different times from $t1$ to $t2$. (b′)–(f′) Closed-up temperature distribution images corresponding to the black-dotted rectangular in (b)–(f).

Table 1 Design parameters of heat transfer FDTD simulation.

Materials	Heat capacity (J/kg · K)	Thermal conductivity (W/mK)	Density (kg/m^3)
Aluminum	900	238	2700
Egg white	2600 to 3700	0.4 to 0.6	1023 to 1145.5

conditions, we have selectively used proper values according to the temperature level. The initial temperature and heating temperature were set at 25°C and 120°C, respectively.

2.4 *Speckle Variance and Cross-Correlation Calculation*

The speckle variance values were obtained by calculating the interframe variance (SV_{ijk}) of the number (N) of B-scan OCT structural pixel intensity (I_{ijk}) at the same region of interest based on the following equation:

$$SV_{ijk} = \frac{1}{N}\sum_{i=1}^{N}\left[I_{ijk}(x,z) - \frac{1}{N}\sum_{i=1}^{N} I_{ijk}(x,z)\right]^2 = \frac{1}{N}\sum_{i=1}^{N}(I_{ijk} - I_{\text{mean}})^2, \quad (1)$$

i, j, and k indicate the indices of B-scan image, lateral location, and depth location of B-scan images, respectively. N is the number of B-scan images used in speckle variance calculation. I_{ijk} means the OCT signal intensity at pixel (j,k) at the i'th B-scan image. I_{mean} is the temporal averaged intensity at the same point. In this experiment, the averaged 100 B-scan images for speckle variance analysis and selected ROIs' pixels were 900×150 along the X- and Z-directions, respectively. To determine the similarity of ROIs in SvOCT images, the cross-correlation coefficient (r) of speckle variances between two SvOCT A-lines in the one SvOCT image was calculated using the following equation:

$$r = \frac{\sum_p (x_p - m_x)(y_{p+q} - m_y)}{\sqrt{\sum_p (x_p - m_x)^2 \cdot \sum_p (y_{p+q} - m_y)^2}}, \quad (2)$$

where m_x and m_y are the averaged values of the selected discrete A-scan data (x_p and y_p). p and q are the indices of A-scan data.

3 Results

3.1 *FDTD Simulation for Heat Transfer and Temperature Distribution*

Figures 2(b)–2(f) summarize the result of the FDTD simulation for the time-resolved temperature distribution and the heat flux.

Figures 2(b′)–2(f′) show magnified images of the black-dotted rectangular region in Figs. 2(b)–2(f). They provide the estimated temperature distribution of the egg white as the temperature increases. Over the elapsed time (from $t1$ to $t5$), the heat flux spreads out from the bottom to the top area, then the whole of the aluminum bowl area reaches a highest temperature level at $t5$ (i.e., 120°C) rapidly. The change of temperature in egg white area was relatively slower than the aluminum bowl area due to its low thermal conductivity. For instance, in Figs. 2(e) and 2(e′), the temperature level of the aluminum bowl already reached the maximum level, but the bottom of the egg white area became only 103.1°C. The simulated temperature distribution range in the egg white area along the depth direction at $t1$, $t2$, $t3$, $t4$, and $t5$ are 58.2°C to 35.6°C, 78.4°C to 47.1°C, 94.5°C to 52.7°C, 103.1°C to 56.8°C, and 116.8°C to 72.1°C, respectively.

3.2 *OCT and SvOCT Images as a Function of Heating Temperatures*

Figure 3 shows intensity-based B-scan OCT images (a) and SvOCT images (b) of egg white during the heating. As shown in Fig. 3(a), as temperature increased, the thin coagulated protein layer on the surface region became thicker. Additionally, OCT intensity became increased from the bottom since 61.5°C and then the whole OCT imaging area became bright due to the enhancement of OCT intensity since 83.8°C. In the SvOCT images [Fig. 3(c)], there were no changes of speckle variance at 53.4°C and 59.0°C without an OCT intensity saturated area. However, increase of the speckle variance signals was detected in the bottom of the SvOCT image at 61.5°C. By increasing temperature, increased areas of the speckle variance signals were extended to the whole imaging area.

3.3 *Quantitative Analyses*

Figure 4(a) shows five ROIs selected in the SvOCT image at 76.4°C. Five yellow dotted squares indicate different depth ROIs. To avoid the influence of a saturated OCT intensity signal on the surface, the surface area (i.e., 0 to 150 μm) was excluded in quantification analysis. From 150 μm below the surface, we divided five ROIs with the same depth range (i.e., 150 μm). Then, we extracted the averaged value, the standard deviation of OCT signal, speckle variance, and cross-correlation coefficient in each five ROIs. First of all, the OCT intensity enhancement at different ROIs was investigated [Fig. 4(b)]. The OCT intensity in the whole area showed approximately 400% enhancement while increasing temperature. Especially, the OCT intensity in ROI5 increased much faster than in the other ROIs from 61.5°C to 81.8°C. In contrast, the OCT intensity in ROI1, ROI2, and ROI3 were relatively maintained by 76.4°C. Then, the OCT intensity in ROI2 and ROI3 suddenly increased at 78.4°C. In particular, the OCT intensity in ROI1 increased only after reaching 81.8°C. Above 81.8°C, OCT intensity in all ROIs showed increased signal trend.

Figure 4(c) shows the speckle variance enhancement in five ROIs as a function of temperature. From the result, we can classify three stages. The different speckle variance-enhancing patterns were observed at each stage. Speckle variance enhancement in all ROIs increased up to 20% in this stage. In stage 2 (i.e., 59.0°C to 78.4°C), three different speckle variance-enhancing patterns appeared at each ROI. Speckle variances of all ROIs showed early enhancement at 61.5°C from the bottom area. Measured speckle variance enhancement at 61.5°C in ROI1, ROI2, ROI3, ROI4, and ROI5 were $83.2 \pm 7.5\%$, $79.7 \pm 7.4\%$, $101.9 \pm 9.7\%$, $117.6 \pm 10.2\%$, and $161.8 \pm 13.1\%$, respectively. As temperature increased, only the speckle variance signal in ROI4 and ROI5 (i.e., 600 to 900 μm) increased, generally by 78.4°C. The enhanced speckle variances at 78.4°C were measured as $523.2 \pm 46.6\%$ and $552.2 \pm 43.5\%$, respectively. Meanwhile, the speckle variance enhancement in ROI2 and ROI3 (i.e., 300 to 600 μm) remained almost constant and decreased slightly until reaching 76.4°C. The maintained values at 76.4°C in ROI2 and ROI3 are $111.3 \pm 8.2\%$ and $182.1 \pm 17.3\%$, respectively. After arriving at 78.4°C, these speckle variance signals suddenly increased by $376.7 \pm 30.1\%$ and

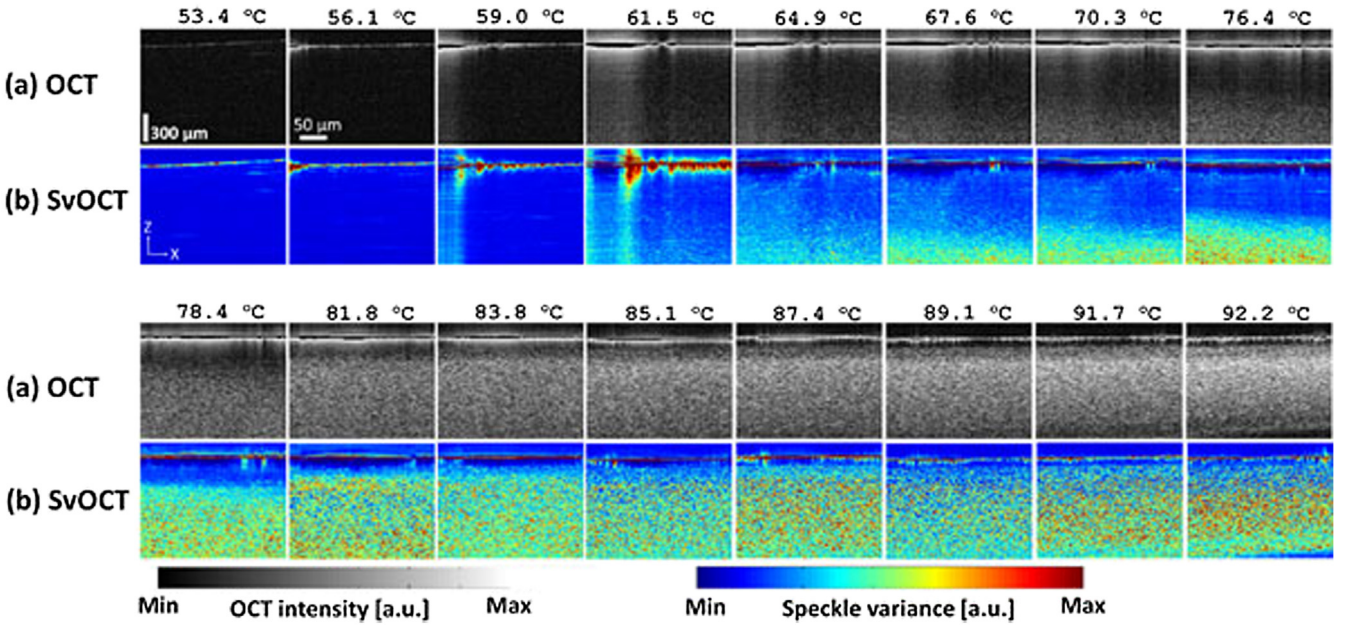

Fig. 3 (a) Normal intensity-based OCT images and (b) corresponding SvOCT images of normal egg white during 16 different heating temperatures from the bottom.

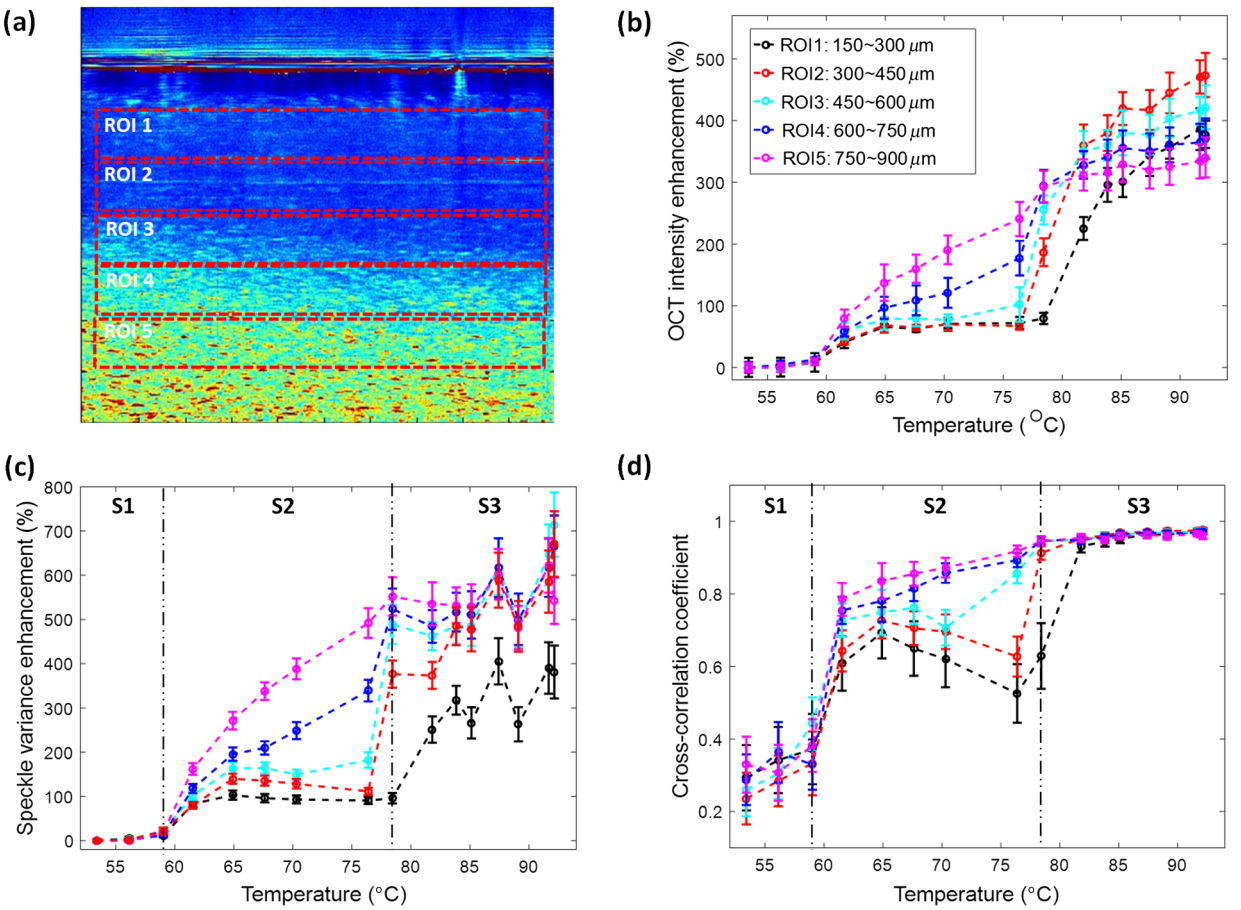

Fig. 4 Analysis of ROIs at 16 heating temperatures. (a) Five selected ROIs in the SvOCT image at 76.4°C. (b) OCT intensity enhancement, (c) speckle variance enhancement, and (d) cross-correlation coefficient at five selected ROIs during 16 heating temperatures. ROI, region of interest; S1, stage 1; S2, stage 2; and S3, stage 3.

488.7 ± 44.3%, respectively. However, the speckle variance signal in ROI1 (i.e., 150 to 300 μm) did not increase by 78.4°C. The measured speckle variance enhancement at 78.4°C was 95.9 ± 11.9%. In stage 3 (i.e., 78.4°C to 92.2°C), speckle variances in all ROIs showed a fluctuation and saturated signal-enhancing pattern. In particular, speckle variance signals in ROI1 showed an increase only from 81.8°C (251.1 ± 29.7%) to 83.8°C (317.6 ± 32.6%), and then fluctuated and saturated.

Figure 4(d) shows the calculated cross-correlation coefficient at five ROIs at different heating temperatures. This result was consistent with the speckle variance changes; however, several different patterns were detected. These values also were classified as three stages. In stage 1 (i.e., 53.4°C to 59.0°C), small increases of the cross-correlation coefficient values were captured in all ROIs. The calculated coefficient values at 59.0°C in ROI1, ROI2, ROI3, ROI4, and ROI5 were 0.37 ± 0.09, 0.33 ± 0.08, 0.44 ± 0.07, 0.33 ± 0.07, and 0.38 ± 0.08, respectively. There was a 17% enhancement in value compared with the initial coefficient value. In stage 2 (i.e., 59.0°C to 78.4°C), although there were different degrees of increase in absolute coefficient values at each ROI, the cross-correlation coefficients in all ROIs suddenly increased from 59.0°C to 61.5°C. The cross-correlation coefficient values at 61.5°C in each ROI were calculated as 0.61 ± 0.07, 0.64 ± 0.06, 0.72 ± 0.05, 0.75 ± 0.04, and 0.79 ± 0.05, respectively. There was approximately 90% enhancement compared with the values at 59.0°C. Then, the cross-correlation coefficient values in ROI4 and ROI5 showed a generally increased pattern by 78.4°C. They were calculated as 0.95 ± 0.02 and 0.94 ± 0.03, respectively, which almost closed to "1." The cross-correlation coefficient values in ROI1, ROI2, and ROI3, however, showed different changing patterns. The coefficient value of ROI3 had a totally increased pattern by 78.4°C (0.94 ± 0.01) with a small signal dropping at 70.3°C (0.71 ± 0.05). The correlation values in ROI1 and ROI2 showed increased values at 64.9°C (ROI1, 0.69 ± 0.07; ROI2, 0.73 ± 0.05) and decreased values at 76.4°C (ROI1, 0.53 ± 0.08; ROI2, 0.63 ± 0.05). Then, they finally increased with different increasing slopes at 78.43°C (ROI1, 0.63 ± 0.09; ROI2, 0.91 ± 0.02). In stage 3 (i.e., 78.4°C to 92.2°C), all cross-correlation coefficient values of ROIs showed saturation to "1" except the correlation value of ROI1 at 81.8°C (0.93 ± 0.02). After temperature reached 81.81°C, speckle variance of all ROIs showed the saturated pattern, which indicated that the denaturation and coagulation processes were stabilized.

4 Discussion

Changed OCT intensity information can be used to discriminate and assess the structure change in the interested region (i.e., cancerous tumor, blood coagulation);[33,34] however, quantitative analysis based on OCT intensity is limited to relative assessment of change in the tissue morphology and does not provide direct information about the tissue temperature. Thus, we performed

the speckle variance calculation and directly related the value to the tissue temperature.

The change of condition of OCT speckle is an indicator of the status of scatterers within the sample. Therefore, speckle pattern changes over time reflect physical changes of the scatterers.[35] High speckle variances indicate more stabilized molecule movements. Additionally, by calculating the correlation between SvOCT signals, the condition of the scatterers may be estimated. As speckle variances get stabilized and stable—which indicates low activity/movement of the scatterers—the correlation coefficient between the temporally adjacent images approaches to "1." In our case, by tracking speckle variances and calculating their correlation coefficient in different heating temperatures, we can estimate the condition of the inner egg white-induced thermal denaturation and coagulation.

Egg white proteins are composed of approximately ovalbumin (60%), conalbumin (13%), and others.[36] Conalbumin is the earliest heat denaturized egg white protein at 62°C, at which the liquid state of the white egg begins to bond and aggregate through intermolecular interaction. Thus, conalbumin plays an important role in initiating the denaturation and coagulation process of egg white. Ovalbumin is regarded as the crucial composition related to egg white functions. By being exposed to heating, egg white becomes a stabilized gel structure type via intermolecular reactions. Ovalbumin is denatured at 84°C.[37] Therefore, our result—that shows the onset of speckle variance changes at 53°C to 92°C—is consistent with the principal structural rearrangement of egg white protein around 60°C to 90°C.

Based on the FDTD simulation result, which shows temperature distribution in egg white, we can estimate the tissue denaturation since egg white begins the denaturation process above a specific temperature level (i.e., 62°C). In particular, the bottom area of egg white in Figs. 2(b) and 2(b′) reaches to approximately 60°C, which means denaturation and coagulation process begin at the bottom. The middle depth area in Figs. 2(c) and 2(c′) became 61.4°C, which implies that half of the egg white is denaturalized. Finally, all egg white areas would be denaturalized in Figs. 2(f) and 2(f′). These SvOCT data shown in Fig. 3 consistently demonstrated the same heat transfer result that is estimated in the simulation. Especially, temperature distributions at $t1$ [Figs. 2(b) and 2(b′)] and $t2$ [Figs. 2(c) and 2(c′)] are matched to SvOCT images at 64.9°C and 76.4°C in Fig. 3(b).

OCT intensity images at different heating temperatures [Fig. 2(a)] and quantitative analysis at different ROIs [Fig. 3(b)] show the signal enhancement by increasing the temperature. As small compositions in egg white were aggregated and bonded after 62°C, the size of scatterers in the egg white enlarged, which induced enhancement of the OCT intensity signal by about 400%. Thus, OCT intensity images in Fig. 2(a) can estimate the distribution of the thermal stress inner egg white as depth-resolved information. The OCT intensity enhancement extended to the whole imaging area from the bottom. Additionally, OCT intensity-enhancing profiles [Fig. 3(b)] in a specific temperature range (i.e., 59.0 to 78.4°C) also showed similar signal enhancement at different depths. However, there were inconsistent changes of OCT intensity at different ROIs above 81.8°C. Additionally, the egg white changed from transparent tissue to highly scattering white, which greatly influenced the OCT intensity change. Thus, OCT intensity-based tissue change estimation was not sufficient for proper assessment of the egg white denaturation and coagulation process.

SvOCT images [Fig. 2(b)] with different heating temperatures can also provide the distribution of thermal stress in egg white. As heating temperature increased, the early denaturation was observed in the bottom area at 61.5°C. Then, the denaturation and coagulation process spread throughout the whole imaging area at 83.8°C and stabilized at the above temperatures. From two different quantitative analyses [Figs. 3(c) and 3(d)], we can acquire more detailed denaturation and coagulation process information at different depth ROIs by dividing three stages. In stage 1 (i.e., 53.4°C to 59.0°C), even though there were no significant enhancements of speckle variance (20%) and cross-correlation coefficient (17%) in both results, small signals and values enhancement could be regarded as the initial preparation state for denaturation. In stage 2 (i.e., 59.0°C to 78.4°C), speckle variance in all ROIs started to show speckle variance changes at 61.5°C, and the values of the cross-correlation coefficient also changed with 90% enhancement at 61.5°C compared to the previous temperature (i.e., 59.0°C). These results almost matched the starting temperature of conalbumin denaturation (i.e., 62°C). The speckle variance and coefficient value in ROI4 and ROI5 showed a generally increasing trend by 78.4°C, which implies the smooth change of characteristics of the egg white compositions in 600 to 900 μm. In contrast, a sudden increase of speckle variance signal in ROI3 and ROI4 at 78.4°C means that characteristics change in 300 to 600 μm at 78.4°C after the first denaturation process of conalbumin at 61.5°C. Moreover, the cross-correlation values also support this estimation with value decline and increase pattern, which indicates the mixed condition of liquid and gel inner egg white. ROI1's speckle variance maintenance by 78.4°C indicates that the subsurface layer (150 to 300 μm) was less affected by thermal stress. It is also estimated as the mixed condition of liquid and gel as following the cross-correlation coefficient values similar to the changing pattern with ROI2 and ROI3. In stage 3 (i.e., 78.4°C to 92.2°C), all ROIs show speckle variance signal fluctuation and saturated pattern. From these results, we cannot estimate the correct situations of the inner egg white. Fortunately, the cross-correlation values at all ROIs above 81.8°C went to "1." This indicated that the condition of the inner egg white in all ROIs was stabilized. Theoretically, the changes of egg white will be stabilized in these temperature ranges after completing all denaturation and coagulation processes.[37] Therefore, we successfully estimate the states of the inner egg white during increasing temperature using SvOCT images, speckle variance, and cross-correlation coefficient values.

5 Conclusion

We successfully demonstrated that the change of egg white protein denaturation and coagulation processing can be monitored using SvOCT for heating the sample from 53.4°C to 92.2°C. Those results are well matched to previously reported denaturation and coagulation of egg white.[36] Compared to other monitoring methods, our SvOCT method can provide the depth-resolved denaturalized process with a high depth resolution. Moreover, by presenting quantitative analyses of SvOCT images' different depth regions, we validated the performance of SvOCT as a new monitoring tool of the denaturation and coagulation process. Based on our feasibility results, we expect that it will contribute to monitoring several lasers and thermal-induced therapy in clinical fields including dermatology and ophthalmology.[38,39]

Disclosures

No conflicts of interest, financial or otherwise, are declared by the authors.

Acknowledgments

This work was supported by the World Class 300 Project (S2340708, Development of Ophthalmic Multipurpose Glaucoma/Retina Diagnosis/Treatment Integral Laser System) of the Small and Medium Business Administration (SMBA), Republic of Korea.

References

1. M. G. Romanini, "Advances in cell and molecular biology: Volume I. Edited by E. J. DuPraw. New York, London: Academic Press Inc. 308 pp. $15·00," *J. Hum. Evol.* **2**(3), 247–249 (1973).
2. B. Rost, "Review: protein secondary structure prediction continues to rise," *J. Struct. Biol.* **134**(2), 204–218 (2001).
3. C. B. Anfinsen, "Studies on the principles that govern the folding of protein chains" *Science* **181**(20), 223–230 (1972).
4. D. Shortle, "The denatured state (the other half of the folding equation) and its role in protein stability," *FASEB J.* **10**(1), 27–34 (1996).
5. M. Yamasaki, H. Yano, and K. Aoki, "Differential scanning calorimetric studies on bovine serum albumin: I. Effects of pH and ionic strength," *Int. J. Biol. Macromol.* **12**(4), 263–268 (1990).
6. D. Nohara, A. Mizutani, and T. Sakai, "Kinetic study on thermal denaturation of hen egg-white lysozyme involving precipitation," *J. Biosci. Bioeng.* **87**(2), 199–205 (1999).
7. A. Michnik et al., "Comparative DSC study of human and bovine serum albumin," *J. Therm. Anal. Calorim.* **84**(1), 113–117 (2006).
8. B. K. Park et al., "Monitoring protein denaturation using thermal conductivity probe," *Int. J. Biol. Macromol.* **52**, 353–357 (2013).
9. K. Farahani et al., "MRI of thermally denatured blood: methemoglobin formation and relaxation effects," *Mag. Reson. Imaging* **17**(10), 1489–1494 (1999).
10. Z. Ignatova and L. M. Gierasch, "Monitoring protein stability and aggregation in vivo by real-time fluorescent labeling," *Proc. Natl. Acad. Sci. U. S. A.* **101**(2), 523–528 (2004).
11. G. Y. Hou et al., "High-intensity focused ultrasound monitoring using harmonic motion imaging for focused ultrasound (HMIFU) under boiling or slow denaturation conditions," *IEEE Trans. Ultrason. Ferroelectr. Freq. Control* **62**(7), 1308–1319 (2015).
12. D. Huang et al., "Optical coherence tomography," *Science* **254**(5035), 1178–1181 (1991).
13. J. Lee et al., "Decalcification using ethylenediaminetetraacetic acid for clear microstructure imaging of cochlea through optical coherence tomography," *J. Biomed. Opt.* **21**(8), 081204 (2016).
14. E. Sattler, R. Kästle, and J. Welzel, "Optical coherence tomography in dermatology," *J. Biomed. Opt.* **18**(6), 061224 (2013).
15. R. F. Spaide and C. A. Curcio, "Anatomical correlates to the bands seen in the outer retina by optical coherence tomography: literature review and model," *Retina* **31**(8), 1609–1619 (2011).
16. P. A. Testoni and B. Mangiavillano, "Optical coherence tomography in detection of dysplasia and cancer of the gastrointestinal tract and biliopancreatic ductal system" *World J. Gastroenterol.* **14**(42), 6444–6452 (2008).
17. M. Villiger et al., "Deep tissue volume imaging of birefringence through fibre-optic needle probes for the delineation of breast tumour," *Sci. Rep.* **6**, 28771 (2016).
18. A. Nemeth et al., "Optical coherence tomography-applications in nondestructive testing and evaluation," Chapter 9, in *Optical Coherence Tomography*, pp. 163–186, INTECH Open Access Publisher (2013).
19. V. V. Tuchin, *Handbook of Coherent-Domain Optical Methods: Biomedical Diagnosis, Environmental Monitoring, and Materials Science*, Springer, New York (2013).
20. N. H. Cho et al., "Quantitative assessment of touch-screen panel by nondestructive inspection with three-dimensional real-time display optical coherence tomography," *Opt. Lasers Eng.* **68**, 50–57 (2015).
21. M. Sabuncu and M. Akdoğan, "Photonic imaging with optical coherence tomography for quality monitoring in the poultry industry: a preliminary study," *Rev. Bras. Ciênc. Avíc.* **17**(3), 319–324 (2015).
22. B. Choi et al., "Use of optical coherence tomography to monitor biological tissue freezing during cryosurgery," *J. Biomed. Opt.* **9**(2), 282–286 (2004).
23. K. Greco et al., "Accurate prediction of collapse temperature using optical coherence tomography-based freeze-drying microscopy," *J. Pharm. Sci.* **102**(6), 1773–1785 (2013).
24. S. Koinzer et al., "Correlation of temperature rise and optical coherence tomography characteristics in patient retinal photocoagulation," *J. Biophotonics* **5**(11–12), 889–902 (2012).
25. S. Seevaratnam et al., "Quantifying temperature changes in tissue-mimicking fluid phantoms using optical coherence tomography and envelope statistics," *Proc. SPIE* **8938**, 89380R (2014).
26. H. Spahr et al., "Imaging of photothermal tissue expansion via phase sensitive optical coherence tomography," *Proc. SPIE* **8213**, 82131S (2012).
27. J. Tucker-Schwartz et al., "In vivo photothermal optical coherence tomography of gold nanorod contrast agents," *Biomed. Opt. Express* **3**(11), 2881–2895 (2012).
28. L. Conroy, R. S. DaCosta, and I. A. Vitkin, "Quantifying tissue microvasculature with speckle variance optical coherence tomography," *Opt. Lett.* **37**(15), 3180–3182 (2012).
29. M. S. Mahmud et al., "Review of speckle and phase variance optical coherence tomography to visualize microvascular networks," *J. Biomed. Opt.* **18**(5), 050901 (2013).
30. K. Zhang and J. U. Kang, "Graphics processing unit accelerated nonuniform fast Fourier transform for ultrahigh-speed, real-time Fourier-domain OCT," *Opt. Express* **18**(22), 23472–23487 (2010).
31. K. Zhang and J. U. Kang, "Real-time intraoperative 4D full-range FD-OCT based on the dual graphics processing units architecture for microsurgery guidance," *Biomed. Opt. Express* **2**(4), 764–770 (2011).
32. J. S. Coimbra et al., "Density, heat capacity and thermal conductivity of liquid egg products," *J. Food Eng.* **74**(2), 186–190 (2006).
33. E. C. Cauberg et al., "Quantitative measurement of attenuation coefficients of bladder biopsies using optical coherence tomography for grading urothelial carcinoma of the bladder," *J. Biomed. Opt.* **15**(6), 066013 (2010).
34. X. Xu, J. Lin, and F. Fu, "Optical coherence tomography to investigate optical properties of blood during coagulation," *J. Biomed. Opt.* **16**(9), 096002 (2011).
35. J. M. Schmitt, S. Xiang, and K. M. Yung, "Speckle in optical coherence tomography," *J. Biomed. Opt.* **4**(1), 95–105 (1999).
36. E. D. N. S. Abeyrathne, H. Y. Lee, and D. U. Ahn, "Egg white proteins and their potential use in food processing or as nutraceutical and pharmaceutical agents—a review," *Poult. Sci.* **92**(12), 3292–3299 (2013).
37. J. W. Donovan et al., "A differential scanning calorimetric study of the stability of egg white to heat denaturation," *J. Sci. Food Agric.* **26**(1), 73–83 (1975).
38. M. S. Blumenkranz, "The evolution of laser therapy in ophthalmology: a perspective on the interactions between photons, patients, physicians, and physicists: the LXX Edward Jackson memorial lecture," *Am. J. Ophthalmol.* **158**(1), 12–25.e1 (2014).
39. D. Hawkins and H. Abrahamse, "Effect of multiple exposures of low-level laser therapy on the cellular responses of wounded human skin fibroblasts," *Photomed. Laser Ther.* **24**(6), 705–714 (2006).

Changho Lee has been a postdoctoral fellow at Johns Hopkins University (JHU) in Baltimore, USA, since 2016. Before joining JHU, he studied at the Kyungpook National University for his PhD degree. Recently, he investigated at the Pohang University of Science and Technology (POSTECH) as the postdoctoral fellow and research assistant professor. He focused on developing biomedical imaging modalities, such as optical coherence tomography, photoacoustic imaging, integrated optical imaging, and intraoperative surgical imaging.

Gyeongwoo Cheon received his PhD in electrical and computer engineering from JHU in 2016. He is currently an advanced computing engineer at GE global research center. He was conducting research on developing robot-assisted microsurgical tools based

on optical coherence tomography under Dr. Jin U. Kang with Photonics and Optoelectronics Lab during his PhD degree.

Do-Hyun Kim received his PhD in physics in 2000 from Seoul National University, and in engineering in 2006 from the JHU. He worked for US Food and Drug Administration from 2006 to 2016. He served as a research professor at Catholic University of Korea in 2016. He is currently managing BT Solutions, Inc., Solutions for BT, LLC., and S&E Medical, Inc.

Jin U. Kang is Jacob Suter Jammer professor of the Department of Electrical and Computer Engineering, and Department of Dermatology at the JHU. He has published more than 160 journal papers and contributed to over 220 conference proceedings in the field of fiber optic devices and systems, OCT and optical imaging systems, nonlinear optics, and microwave-photonics. He is fellow of OSA, SPIE, and of American Institute for Medical and Biological Engineering.